Design and Analysis of a Microwave-Optical Dual Modality Biomolecular Sensing Platform

Luya Zhang, *Student Member, IEEE,* and Ali M. Niknejad, *Fellow, IEEE*

***Abstract*—A combined microwave-optical biomolecular sensor with high sensitivity and selectivity is presented. The microwave sensor characterizes the dielectric properties of a medium using the oscillation frequency shift. To improve the sensor sensitivity beyond the $1/f^3$ phase noise limit, a quadrature-oscillator-based reactance sensing scheme is proposed, which attenuates the $1/f^3$ noise by 20 dB/dec. Further sensitivity enhancement is realized by a novel chopping technique which modulates the free-running frequencies of the coupled oscillators differentially while maintaining a fixed locking frequency. To achieve a higher selectivity, optical sensors are introduced to target for specific biomolecules. Utilizing single photon avalanche diodes, they detect both photon intensity and photon emission time. A biosensor prototype was fabricated in a 28 nm CMOS technology. The microwave sensor achieves 0.2 ppm/$\sqrt{\text{Hz}}$ frequency sensitivity with 11.5 mW power consumption. The optical sensor shows 500/second dark count rate and 300 ps timing jitter at 1 V excess bias. A protein thermal denaturation experiment confirms the sensitivity and selectivity enhancement of the dual-modality biosensing platform.**

***Index Terms*—Biological and chemical sensors, multiparametric, millimeter-wave circuits, injection lock, quadrature generation, dielectric spectroscopy, single photon avalanche diodes.**

I. Introduction

HIGHLY sensitive and selective detection of biomolecules and their interactions plays a central role in the promises of precision medicine, drug discovery and many other clinical areas. The sensitivity of a biosensor can be improved by minimizing sensor noise and interferences, while the selectivity of a biosensor relies primarily on the specific binding process, e.g. antibody-antigen reaction, often not achievable due to the high analyte similarities in a complex biomedium [1].

Fortunately, advances in lab-on-chip techniques permit the integration of multiparametric biosensors to create a multi-dimensional fingerprint for the target analytes, which enhances the sensor selectivity and classification capabilities greatly [2]–[4]. For instance, [2] developed a dual-modality microfluidic device, which measures cell elongation length, deformability and electrical impedance to better classify different types of cells. A further step towards lab-on-CMOS [5]–[10] offers a complete system integration on a miniaturized platform to reduce parasitics and interferences. More importantly, various signal processing techniques can be applied *in situ* to enhance the sensor sensitivity. Examples include chopper stabilization in a flow cytometer [11] to alleviate sensor offsets and flicker noise, correlated double sampling (CDS) in a bioluminescence chip [12] to suppress the dark current, and Σ-Δ modulation in a fluorescence DNA chip [13] to extend the dynamic range.

This work was supported by the National Science Foundation Division of Electrical, Communications and Cyber Systems (ECCS) under Grant No.1608958.

The authors are with the Electrical Engineering and Computer Sciences, University of California, Berkeley, CA 94720 USA (e-mail: luyazhang@berkeley.edu).

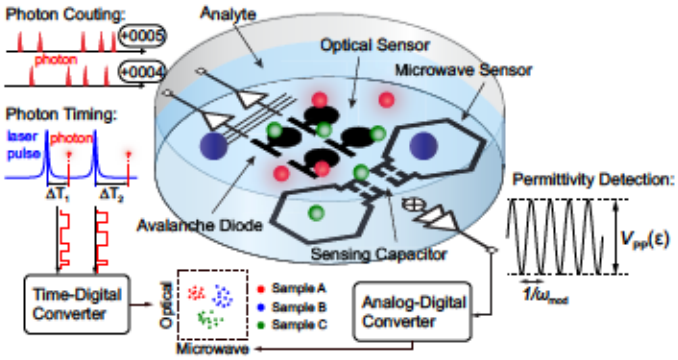

Fig. 1. Proposed dual-modality microwave-optical biomolecular sensor.

Despite the numerous benefits, lab-on-CMOS integration of highly sensitive multimodal biosensors sufficient for biomolecular detection remains an issue. The challenge is that different sensing modalities favor different and sometimes contradictory fabrication recipes for sensitivity enhancement. For example, microwave spectroscopies (dielectric [14]–[17], magnetic [18], molecular rotational [19]) benefit from deep-submicron MOSFETs with higher f_T and lower parasitics, while photodetectors exhibit better performance metrics (e.g. quantum efficiency) [20]–[22] in the conventional technology nodes with lower doping levels and wider depletion regions. Moreover, extra post processing required by one modality could interfere with the operation of others. For example, depositing optical filter layers on top of the chip surface desensitizes near-field sensors.

To address these challenges, we demonstrated a microwave-optical biomolecular sensor in a 28 nm CMOS process [23]. Quadrature locked oscillators (QVCOs) are used for highly sensitive dielectric sensing at microwave frequencies (40 GHz) to bypass the parasitic interfacial polarization at the sensor-water interface [24], [25]. Meanwhile, single photon avalanche diodes (SPADs) are introduced to compensate for the reduced quantum efficiency in such an advanced process. They measure bioluminescence intensity and fluorescence lifetime in a time-gated fashion [26]–[28], which eliminates optical filters and avoids dielectric sensor desensitization. Expanded from [23], this paper presents a complete design analysis with more measurement results. In the case of the microwave sensor, [23] identifies flicker noise as the primary sensitivity limit and uses CDS to suppress it, but at the expense of noise aliasing. Here the source of flicker noise is investigated and a novel chopping

TABLE I
SYSTEM SPECIFICATIONS

	Microwave Sensor	Optical Sensor
Transducer Type	Oscillator	Avalanche Diode
Signal Type	Permittivity	Fluorescence Lifetime
Signal Level	$\Delta\epsilon = 0.1\%$ ($\epsilon_{water} = 20$ [29])	$\tau = 1-30$ ns [26]
Noise Requirement	$(f_n/f)_{rms} < 4$ ppm	$t_{jitter} < 0.5$ ns

technique is proposed to improve the sensitivity without noise folding penalty.

This paper is organized as follows. The system architecture and specifications to satisfy biomolecular sensing requirements are provided in Section II. Section III and IV discuss the detailed design considerations of the two sensing modalities, respectively. The electrical and biological measurement results are presented in Section V and VI.

II. System Architecture and Specification

Fig. 1 illustrates the system-level diagram of the microwave-optical biosensing platform. The microwave sensor utilizes a pair of sensing capacitors as part of the QVCO tank to detect the analyte permittivity. As shall be shown in the next section, compared with a single oscillator or in-phase coupled oscillators, using QVCOs accompanied by the proposed readout scheme increases the sensor sensitivity. Meanwhile, the SPAD-based optical sensors detects the bioluminescence intensity and fluorescence lifetime to further improve the sensor selectivity. A SPAD can be viewed as an optical latch, which is triggered upon a photon absorption, so that both photon quantities and their arrival times can be measured.

To allow detection of biomolecules and their interactions, Table I lists the design specifications for each sensing modality. The minimal signal level during the biomedium analysis determines the sensor noise floor. Based on EM simulations, 1% of $|\Delta\epsilon|$ in an aqueous solution (at 40 GHz, $\epsilon_{water} = 20$) leads to $|\Delta C| = 5.22$ aF. With 54 fF total tank capacitance in this design, a 4.83 ppm frequency change needs to be resolved for measurement of 1% dielectric change with 20 dB SNR, or 0.1% change with 0 dB SNR, which sets the sensor noise floor. Similarly, since the typical fluorescence lifetimes of standard dyes are 1–30 ns, the timing jitter of the optical sensor should be kept below 0.5 ns, i.e., half of the minimal lifetime.

III. QVCO-based Permittivity Sensor

A. Sensing Scheme

Oscillators are particularly popular in above-GHz reactance sensing [30]–[33] through the measurement of the oscillation frequency shift. As analyzed in [34], the oscillator $1/f^3$ phase noise limits the minimum detectable signal (MDS) and affects the long-term frequency stability. To suppress the $1/f^3$ phase noise, [34] introduced a correlated double counting (CDC) technique [see Fig. 2(a)], where a replica reference tank is added and shares the same active core with the sensing tank to form two oscillators with correlated $1/f^3$ phase noise. The noise can be attenuated by switching between the two tanks and taking the frequency difference. However, CDC faces two

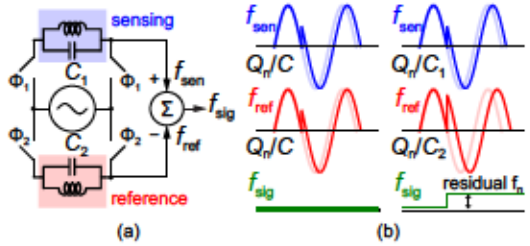

Fig. 2. Oscillator-based sensor using CDC to attenuate $1/f^3$ phase noise. (a) Sensor architecture, and (b) CDC efficiency for $C_1 = C_2$ (left) and $C_1 \neq C_2$ (right). The time-interleaved operation is ignored for illustration simplicity.

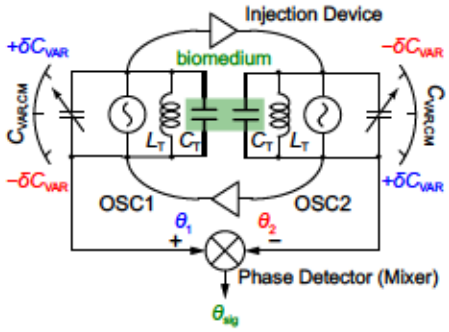

Fig. 3. Proposed permittivity sensor architecture.

major limitations when used in dielectric detection. First, large switches are required to avoid tank quality factor degradation, which in turn contribute excessive capacitive parasitics and decrease sensitivity. Second, to isolate the reference tank from the biomedium, a protection layer (e.g. PDMS, SU-8) must be applied. Since the permittivity of the protection layer ($\epsilon_{PDMS} = 2.3$, $\epsilon_{SU\text{-}8} = 4.1$) is much smaller than water, the two tanks respond differently to the same (correlated) noise charge injection Q_n, as illustrated in Fig. 2(b), which decorrelates the two oscillators and leads to only partial noise cancellation.

Fig. 3 shows the simplified sensing architecture proposed in this work, where the sensing oscillator is divided into two mutually coupled oscillators *equally* exposed to the biomedium. To facilitate measuring the tank capacitance in a $1/f^3$-phase-noise-free regime, an additional varactor is included in each oscillator, and their values are modulated differentially at ω_m,

$$C_{VAR1,2} = C_{VAR,CM} \pm \delta C_{VAR} \cdot \cos(\omega_m t), \tag{1}$$

so that the *free-running* frequencies of the two oscillators are also modulated differentially,

$$\begin{aligned} \omega_{1,2} &= \omega_0\left(1 \mp \frac{\delta C_{VAR}}{2C_T} \cdot \cos(\omega_m t)\right) \\ &= \omega_0 \mp \omega_\Delta \cdot \cos(\omega_m t). \end{aligned} \tag{2}$$

With a shallow modulation depth ω_Δ, injection locking maintains the *operating frequency* of the two oscillators at ω_0 and converts the modulated frequency difference into a differential phase signal, to be measured by the subsequent phase detector. The gist is that the tank capacitance C_T is encoded in the phase signal and is not corrupted by $1/f^3$ phase noise as long as ω_m is beyond the flicker corner frequency ω_C.

The quantitative relationship between the tank capacitance and the phase signal can be established via Adler's equation

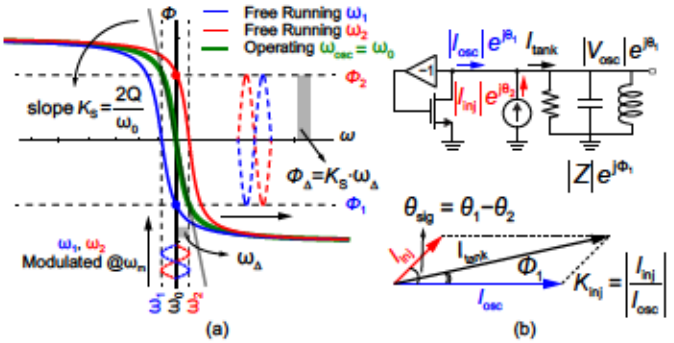

Fig. 4. Proposed sensing scheme. (a) Tank impedance phase spectrum showing the modulation principle, and (b) injection phasor diagram showing $|\theta_{sig}| \approx \Phi_\Delta/K_{inj}$.

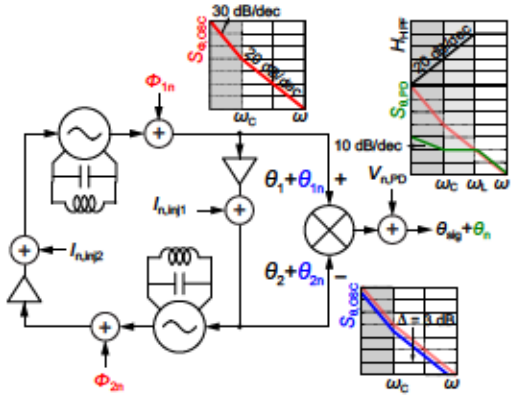

Fig. 5. The noise model of the permittivity sensor.

[35]–[37]. The phase dynamics of an oscillator under injection is given by

$$\frac{d\theta_i}{dt} = \omega_i - \omega_{inj} + K_{inj}\frac{\omega_i}{2Q}\sin(\theta_{inj,i} - \theta_i), \tag{3}$$

where θ_i = oscillation phase, $\theta_{inj,i}$ = injection phase, ω_i = free-running frequency, ω_{inj} = injection frequency, K_{inj} = injection strength, Q = tank quality factor and $i = 1, 2$. At steady state, the two oscillators are locked to ω_{osc} so that $d\theta_i/dt = 0$ and $\omega_{inj} = \omega_{osc}$. Assume the injection signal is in-phase with the injection source, i.e., $\theta_{inj,1} = \theta_2$ and vice versa. It follows from (3) that,

$$\begin{aligned}\omega_{osc} &= \omega_1 + K_{inj}\frac{\omega_1}{2Q}\sin(\theta_2 - \theta_1)\\ &= \omega_2 + K_{inj}\frac{\omega_2}{2Q}\sin(\theta_1 - \theta_2).\end{aligned} \tag{4}$$

Combining (2) and (4) validates that two oscillators lock back to $\omega_{osc} = \omega_0$, and yields the solution to the phase signal θ_{sig}.

$$\omega_{osc} = \frac{2\omega_1\omega_2}{\omega_1+\omega_2} = \omega_0 - \frac{\omega_\Delta^2}{\omega_0}\cos^2(\omega_m t) \approx \omega_0 \tag{5}$$

$$\sin(\theta_{sig}) = \sin(\theta_1 - \theta_2) = -\frac{\delta C_{VAR}}{C_T}\frac{Q}{K_{inj}}\cos(\omega_m t) \tag{6}$$

It is apparent from (6) that the tank capacitance C_T manifests itself through the amplitude of the modulated phase signal, with an amplification factor of $\delta C_{VAR} \cdot Q/K_{inj}$. Consequently, increasing δC_{VAR} and reducing injection strength K_{inj} improve the signal quality, given that the shallow modulation assumption still holds (which sets the limits to δC_{VAR} and K_{inj}).

The proposed sensing scheme is in fact a derivative spectroscopy, which can be visualized in Fig. 4(a). When the two oscillators are injection locked at ω_0 (green), their free-running frequencies are modulated differentially around ω_0 (blue and red), which leads to the tank impedance phases $\phi_{1,2}$ being modulated as well. If ω_Δ is small, the output amplitude ϕ_Δ is proportional to the derivative of the tank impedance phase spectrum, $d\phi/d\omega = 2Q/\omega_0$. Based on the injection phasors in Fig. 4(b), the phase signal θ_{sig} is simply ϕ_Δ boosted by $1/K_{inj}$. That is, by modulating the free-running frequencies of the two coupled sensing oscillators, the biomedium dielectric constant, encoded in the tank impedance phase spectrum, can be measured at a frequency beyond the flicker corner.

B. Noise Analysis

One common fallacy is to presume that the phase noise of the two mutually coupled oscillators are completely cancelled through self-mixing, so that the above modulation technique is unnecessary. Starting from Adler's equation, it shall be shown that injection locking and mixing only performs a first-order high-pass filtering to the $1/f^3$ phase noise, mandating the use of modulation.

Fig. 5 shows the sensor noise model, including the oscillator phase noise (uncoupled), $S_{\phi,OSC1,2}$, injection noise $I_{n,inj1,2}$ and phase detector noise $V_{n,PD}$. Since $I_{n,inj1,2}$ strongly depends on the coupling method and can be absorbed into $S_{\phi,OSC1,2}$, while $V_{n,PD}$ is simply additive, the focus here will be $S_{\phi,OSC1,2}$.

For noise analysis, (3) is perturbed by $\theta_i \Rightarrow \theta_i + \theta_{i,n}$ and $\omega_i \Rightarrow \omega_i + d\phi_{i,n}/dt$, where $\theta_{i,n}$ and $\phi_{i,n}$ $(i = 1, 2)$ are oscillator phase fluctuations with and without injection locking, respectively. At steady state, assuming shallow modulation and in-phase injection, (3) becomes

$$\begin{aligned}\frac{d\theta_{1n}}{dt} &= \omega_1 + \frac{d\phi_{1n}}{dt} - \omega_0 - K_{inj}\frac{\omega_1}{2Q}\sin(\theta_{sig} + \theta_{1n} - \theta_{2n})\\ \frac{d\theta_{2n}}{dt} &= \omega_2 + \frac{d\phi_{2n}}{dt} - \omega_0 + K_{inj}\frac{\omega_2}{2Q}\sin(\theta_{sig} + \theta_{1n} - \theta_{2n}).\end{aligned} \tag{7}$$

Therefore the signal noise $\theta_n = \theta_{1n} - \theta_{2n}$ can be derived as

$$\begin{aligned}\frac{d\theta_n}{dt} &= \frac{d\phi_{1n}}{dt} - \frac{d\phi_{2n}}{dt} - K_{inj}\frac{\omega_0}{Q}\sin(\theta_{sig} + \theta_n) - 2\omega_\Delta\cos(\omega_m t)\\ &\simeq \frac{d\phi_{1n}}{dt} - \frac{d\phi_{2n}}{dt} - K_{inj}\frac{\omega_0}{Q}\theta_n.\end{aligned} \tag{8}$$

Laplace transforming (8) yields

$$\Theta_n(s) = \frac{s}{s+\omega_L}\Big(\Phi_{1n}(s) - \Phi_{2n}(s)\Big), \tag{9}$$

where $\omega_L = K_{inj} \cdot \omega_0/Q$ is the overall lock range [38]. (9) validates such first-order high-pass filtering with $\omega_{3\,dB} = \omega_L$. In other words, mutual coupling only attenuates the $1/f^3$ phase noise in θ_n by 20 dB/dec, and chopping is thereby required for higher sensitivity. Note that mutual injection locking alone does not provide any noise filtering effect, only lowering it by 3 dB, i.e., $S_{\theta,OSC1,2} = S_{\phi,OSC1,2}/2$ [39]. The conceptual noise spectrums are plotted in Fig. 5. For validation, the simulated noise spectrums are shown in Fig. 6.

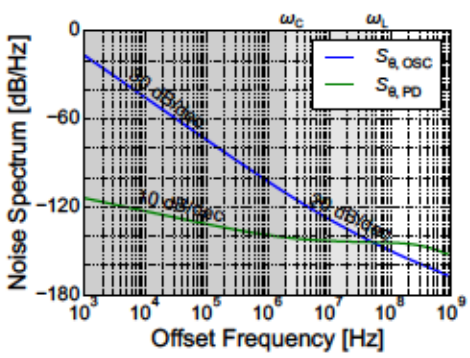

Fig. 6. Simulated noise power spectrum, relative to the carrier (40 GHz) for $S_{\theta,\mathrm{OSC}}$ and DC for $S_{\theta,\mathrm{PD}}$ (ω_C = flicker corner, ω_L = lock range).

C. Circuit Implementation

Fig. 7 shows the complete circuit diagram of the dielectric sensor. The two sensing oscillators are locked in quadrature through a superharmonic coupling network [40]. Compared with coupling at the fundamental output nodes, exploiting second harmonics at the tail nodes preserves sensor sensitivity since it avoids parasitic loading to the sensing tank. Quadrature lock is selected over in-phase lock to maximize the conversion gain for small θ_{sig}. After switching to a QVCO, one needs to examine if the derived equations still hold. This can be done through validation of the only assumption made during the derivation, i.e., in-phase injection ($\theta_{\mathrm{inj,1}} = \theta_2$ and vice versa). Thanks to the superharmonic network, the fundamental injection is delayed by 90° through the inversion of the second harmonic [40]. Suppose the output voltages of IQ oscillators are $\sin(\omega_0 t + \theta_1)$ and $\cos(\omega_0 t + \theta_2) = \sin(\omega_0 t + \theta_2 + 90°)$, respectively (Fig. 7). The signal injected into OscI is thereby $\theta_{\mathrm{inj,1}} = \theta_2 + 90° - 90° = \theta_2$, which validates the assumption.

The operation frequency is designed at 40 GHz (measured 39–42 GHz in water), whereas the proposed topology can be flexibly used for dielectric sensing from a few GHz to tens of GHz. Based on EM simulations, the QVCO tank inductance is $L_\mathrm{T} = 265$ pH with $Q = 12$ in air, and $Q = 9.5$ in phosphate-buffered saline (PBS, $\epsilon_\mathrm{r} = 20$, $\sigma_0 = 2$ S/m). With 1% $\Delta\epsilon_\mathrm{r}$ in PBS, each oscillator picks up 5.22 aF ΔC (out of $C_\mathrm{T} = 54$ fF), creating 48.3 ppm frequency shift. The signal is chopped by modulating the individually accessible varactor control voltages differentially at ω_m around a common bias $V_{\mathrm{VAR,CM}}$. The modulated phase signal θ_{sig} is detected by a double balanced voltage commutating passive mixer. Unlike a Gilbert mixer, passive mixers can be biased at zero DC current to eliminate flicker noise contribution. Since the mixer input impedance is signal dependent, a tuned buffer is inserted between the mixer and QVCO to provide isolation. The mixer is followed by a VGA (1–40 dB), which is wrapped by a pair of chopping switches so that the major $1/f$ noise contributor (QVCO or VGA) can be identified.

IV. SPAD-based Optical Sensor

Despite the superior sensitivity offered by oscillator-based permittivity sensors [14]–[16], [41], they suffer from poor selectivity due to the lack of specific dielectric labels. Since many biomolecular interactions involve light emission with rich information, adding optical sensors helps to improve the selectivity. Compared with conventional photodiodes, SPADs are favored as they can also resolve photon arrival times with sub-ns precision.

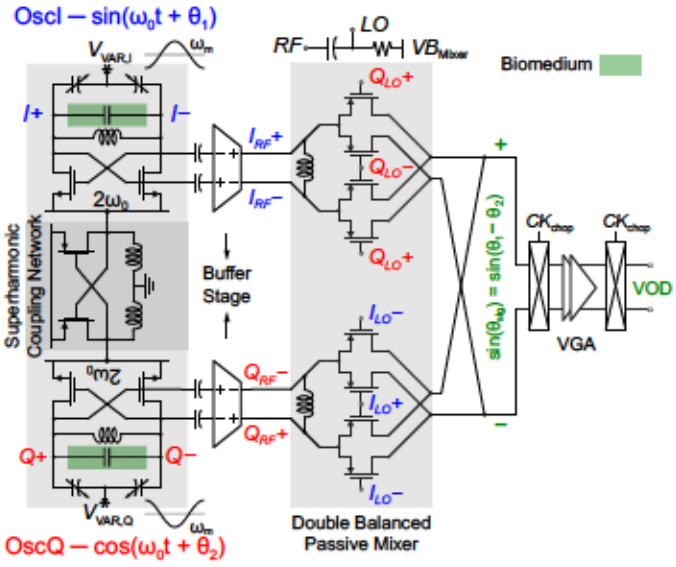

Fig. 7. Permittivity sensor circuit block diagram.

A. Device Implementation

A single photon avalanche diode is a p-n junction reversely biased over its breakdown voltage V_BD by V_EX (the excess bias voltage). Upon absorption of a photon, a substantial amount of current is created through impact ionization. With proper control logic, a digital transition edge is triggered at the onset of breakdown. The avalanche process is then quenched to allow detection of the next photon. Important performance metrics of SPADs are dark count rate (DCR), photon detection efficiency (PDE) and impulse response. A higher V_EX improves both PDE and impulse response, to the extent where the simultaneously increased DCR starts impairing SNR. In advanced processes, transistor oxide breakdown voltages limit V_EX as well.

Fig. 8 shows the cross-section view of the fabricated SPAD in 28 nm CMOS. The multiplication region is formed with p-well/deep n-well, surrounded by a native p-substrate region as the guard ring. Highly doped layers should be avoided as they increase DCR and even promote tunnelling breakdown (not photon-sensitive) due to the increased defect density. The relatively stronger electric field at the edge of the junction can cause premature breakdown [42], which pushes the photon-sensitive region back to the thin junction borderline. A lower-doped guard ring is thereby employed to reduce the edge field. The device is circularly shaped for the same reason to prevent strong corner fields, which forms a 6×6 $\mu\mathrm{m}^2$ multiplication region. The multiplication region is free of the poly-Si layer (fabricated as SiGe or metal in advanced processes) to avoid PDE reduction, which prevents making large-area SPADs due to the strict poly-Si density design rule.

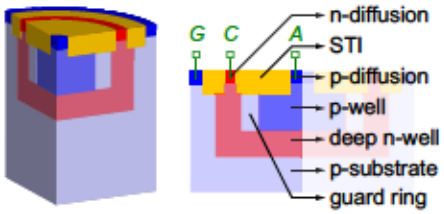

Fig. 8. Cross-section view of the fabricated SPAD. The three contacts are A = anode, external node to a high voltage bias (negative) V_A, C = cathode, internal node (V_C in Fig. 9) to the readout circuit, and G = ground.

B. Circuit Implementation

SPADs are biased at a high negative voltage V_A through the anodes to operate in the Geiger mode. The schematic of the pixel-level control logic and the signal timing diagram are shown in Fig. 9. V_{EX} is defined through $V_{DD}-V_A-V_{BD}$. Thick-oxide transistors are used to interface with SPADs to extend the available V_{EX} to 1.8 V. An external clock *CK* is fed to the chip and generates two non-overlapping phases ϕ_1 and ϕ_2 to activate/deactivate the SPAD periodically. This *CK* can also be synchronized to a pulsed laser to perform fluorescent lifetime measurements. An 8-bit delay unit (Δt = 300 ps) is inserted to allow finer timing alignment.

The pixel control circuit contains three key units: an NMOS quencher M_N, a PMOS pre-charger M_P and an edge-triggered positive feedback loop. The operation principle is as follows. As shown in Fig. 9(b, i), after ϕ_1 turns off M_N, the SPAD is activated by ϕ_2 through M_P. When an avalanche event starts, the current spike begins to discharge the cathode V_C, which reduces the SPAD built-in electric field, avalanche current, and eventually quenches the device. Meanwhile, through the DFF, the falling edge of V_C triggers the positive feedback to turn off M_P and turn on M_N, which expedites the quenching process to sharpen the transition edges. Moreover, the SPAD is kept off until the next activation cycle to prevent afterpulsing (which worsens DCR). If no event occurs during a preset detection window [Fig. 9(b, ii)], ϕ_1 will deactivate the SPAD through M_N. Both V_{Cd} and V_T can be configured for photon counting and photon timing [Fig. 9(b, iii and iv)]. V_{Cd} compares with its leading rising edge to measure photon arrival times, while V_T uses its trailing rising edge (created by the DFF asynchronous set *S*) as the reference. To reduce the counting window size, V_{Cd} is preferred when most photons arrive closer to the beginning of the detection window whereas V_T is better suitable for late photons.

V. Sensor Electrical Characterization

The chip is fabricated in the TSMC 28 nm bulk CMOS process, and occupies 1.2×1.0 mm^2. The prototype contains one QVCO-dielectric sensor and eight SPAD-optical sensors. The sensing capacitors are configured as part of the inductor feeds using top metal layers (M10 and AP). A bio-cavity is created by aligning a slab of drilled Polydimethylsiloxane (PDMS) to the sensor chip on the PCB. Adhesion bonding and mechanical pressure are used to prevent medium leakage. Fig. 10 shows the chip photo and packaging.

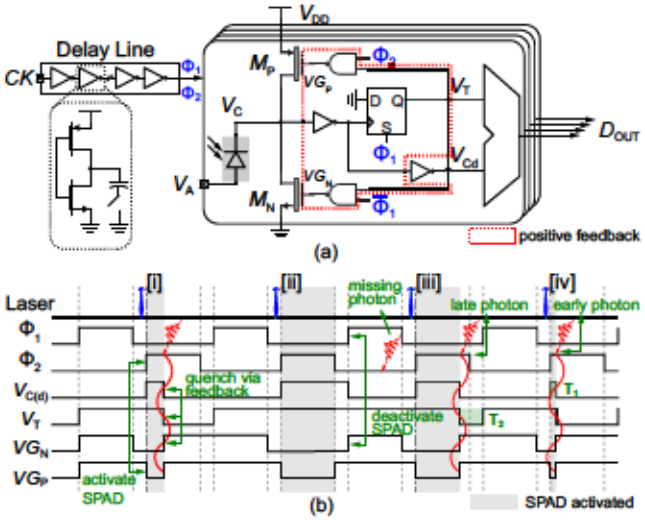

Fig. 9. (a) SPAD circuit block diagram and (b) operation timing diagram.

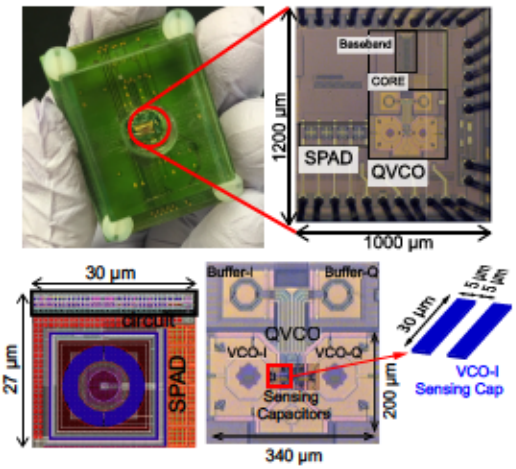

Fig. 10. Chip micrograph and PCB packaging for bio-experiments.

A. QVCO Electrical Characterization

All the electrical characterizations are performed in both air and PBS conditions. The frequency tuning range [Fig. 11(a)] and lock range [Fig. 11(b)] are characterized by coupling the oscillator near-field to a SG probe (Cascade Microtech ACP40-W-SG-150). The signal is then amplified and measured using a spectrum analyzer (Agilent N9030A). When measuring the lock range, the varactor control voltages of IQ oscillators are offset differentially from $V_{VAR,CM}$ by $V_{VAR,DM}$. The value of $V_{VAR,DM}$ when pulling is observed denotes the lock range.

To validate the noise analysis and prove the necessity of modulation, the major flicker source is sorted out by inspecting the sensor output noise spectrums as follows. First, the noise spectrums are measured when the VGA chopper pair (Fig. 7) is enabled (at 10 MHz) and disabled (both with $V_{VAR,DM}$ = 0). As shown in the top subplot of Fig. 12, the contribution of the VGA flicker noise is imperceptible. For further verification, the noise spectrum of the VGA alone was also measured and shown in the bottom subplot of Fig. 12, which is indeed much lower than the overall sensor noise level. However, once the

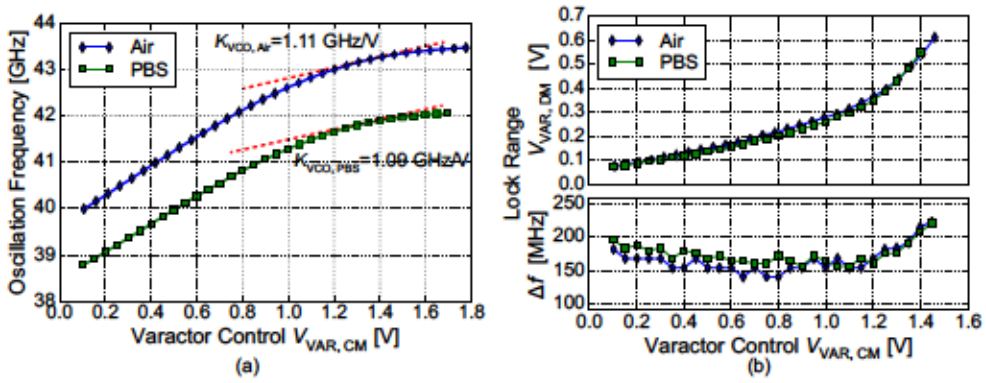

Fig. 11. Measured QVCO (a) frequency tuning range and (b) lock range, denoted by (top) varactor control voltage difference at the edge of lock, and (bottom) the correspondent frequency reduction from the nominal oscillation frequency, as predicted by (5).

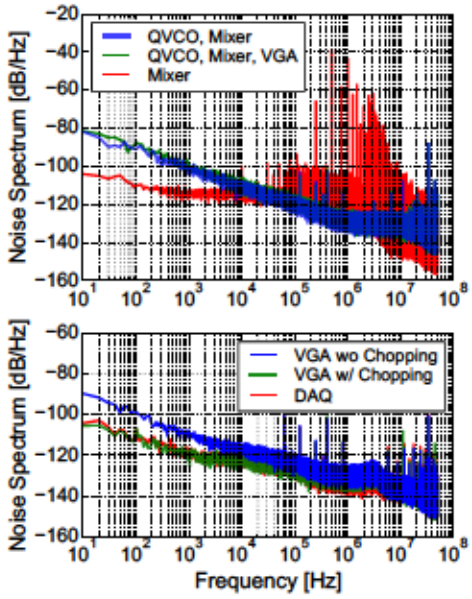

Fig. 12. Measured output noise spectrums: (top) the entire permittivity sensor, when (blue) in lock & chopper on, (green) in lock & chopper off and (red) out of lock; and (bottom) VGA only, where the residual flicker noise comes from the off-chip data acquisition tool (DAQ).

two oscillators are unlocked with a large $V_{VAR,DM}$, the output noise spectrum, down-converted from the oscillator far-out f^0 phase noise [43], is flattened out, indicating that the QVCO virtually contributes all the flicker noise. This is expected since the QVCO transistor size is much smaller than the VGA.

Chopping is performed by modulating the varactor control voltages differentially with $\delta_m \cdot \cos(\omega_m t)$ around a common bias $V_{VAR,CM} = 1.35$ V. The modulation frequency is 1 MHz, above the flicker noise corner (about 900 kHz, Fig. 12). The optimal modulation depth should be the largest δ_m that satisfies shallow modulation requirements to ensure good linearity and close-in noise performance. Specifically, according to (6), a large δ_m (large δC_{VAR}) is desirable for a higher signal gain. However, as δ_m increases, the second-order nonlinear term $-\frac{\omega_\Delta^2}{\omega_0}\cos^2(\omega_m t)$ in (5) becomes appreciable, which causes the oscillation frequency to drop [see Fig. 13(a)]. Moreover, it also modulates the locking frequency at $2\omega_m$ and distorts the output waveform severely [Fig. 13(b)], as the two oscillators cannot lock to a fixed frequency but a variable one. Another impediment that arises from the modulation of the locking frequency is flicker noise up-conversion. As shown in Fig. 14, when $\delta_m = 50$ mV, although the overall noise spectrum seems unaltered, the close-in band (shaded area) incurs clear flicker noise up-conversion, which counteracts the benefits of a higher signal gain and degrades the SNR. $\delta_m = 10$ mV is selected as a good compromise.

To characterize the sensor sensitivity in terms of $\delta f/f_0$ from the measured noise spectrum, $V_{VAR,CM}$ is employed as an intermediate variable, as adapted from [11]. Denote the VGA output as $V_{OD} = S_m \cdot \cos(\omega_m t)$. The following two quantities,

$$K_{VCO} = \frac{\partial f_0}{\partial V_{VAR,CM}},\ K_{TR} = \frac{1}{\delta_m}\frac{\partial S_m}{\partial V_{VAR,CM}} \tag{10}$$

are measurable from the frequency tuning curve [Fig. 11(a)] and the modulation gain plot [Fig. 15(a)]. The measured noise v_n in S_m can thereby be converted to the frequency noise f_n through a simple division,

$$f_n = \frac{K_{VCO}}{K_{TR}}\frac{v_n}{\delta_m/\sqrt{2}} \tag{11}$$

Normalizing f_n by f_0 gives the frequency sensitivity. As shown in Fig. 15(b), the thermal noise limited MDS is 0.2 ppm/$\sqrt{\text{Hz}}$ for air and PBS. This corresponds to a minimal detectable capacitance change of 0.0216 aF/$\sqrt{\text{Hz}}$ in PBS at 42 GHz. Despite a lower tank Q in PBS, its integrated noise is similar to air, since the QVCO $1/f^2$ noise is filtered out.

The dynamic range of an injection-locked-oscillator based reactance sensor is determined by the lock range [15], [44], which is generally narrow. A feedback-around-sensor structure was utilized in [15] to extend the dynamic range with elevated system complexity. Here both sensing oscillators are equally exposed to the biomedium, so that their oscillation frequencies shift together when there is a dielectric change. The dynamic range is thereby decoupled from the lock range. When the measurement condition changes from air & $V_{VAR,CM} = 1.7$ V to PBS & $V_{VAR,CM} = 0.1$ V [Fig. 11(a)], a frequency shift of 4.7 GHz is supported by the sensing topology, corresponding to a dynamic range of more than 115 dB.

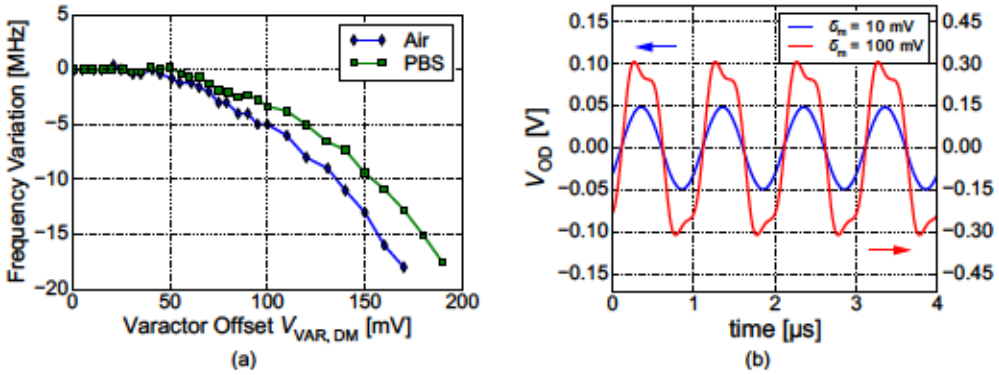

Fig. 13. Measured (a) variation of the oscillation frequency as the varactor control difference increases ($V_{VAR,CM}$ = 1.35 V), and (b) sensor output waveforms.

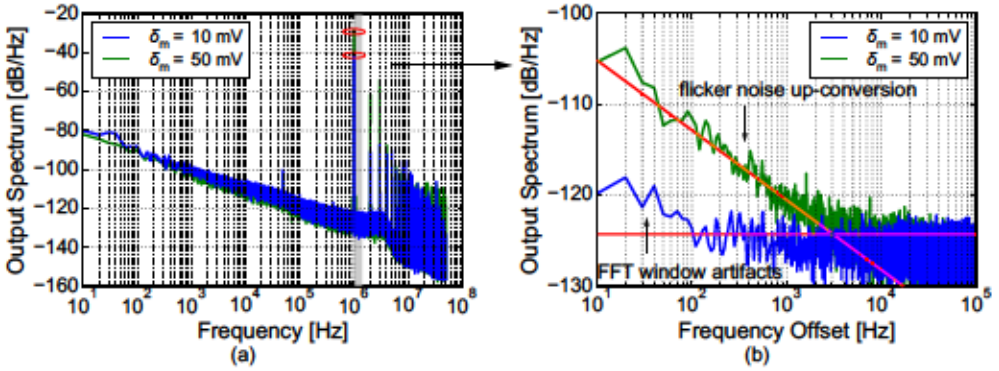

Fig. 14. Measured sensor output spectrum at two different modulation depths, plot relative to (a) DC and (b) the modulation frequency (1 MHz).

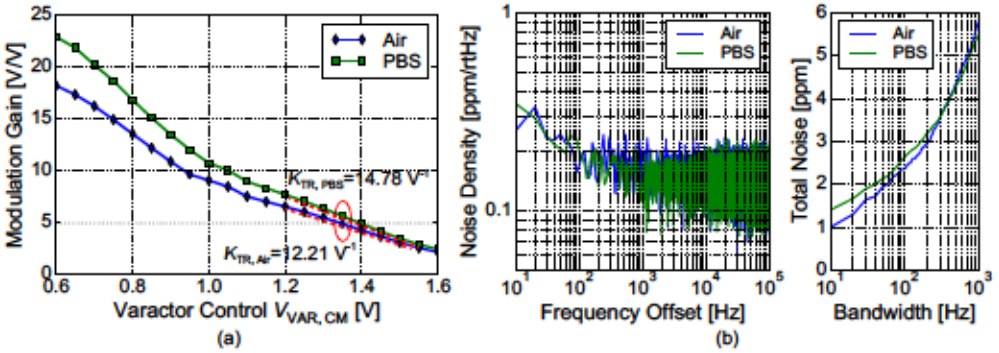

Fig. 15. Measured (a) modulation gain S_m/δ_m, and (b) frequency noise PSD, integrated noise over different filter bandwidths.

B. SPAD Electrical Characterization

The I-V curve of the fabricated SPADs was characterized using a semiconductor analyzer (Keysight B1500A), showing a breakdown voltage of 15.3 V at room temperature.

The dark count rate (DCR) is measured at different excess biases V_{EX} by varying the anode voltage V_A. The SPAD is gated with 70% on-cycle by a 1 MHz *CK* signal [Fig. 9(a)] and an accumulated 10-second measurement is performed to allow a reliable extraction of DCR. The reported DCR in Fig. 16(a) corresponds to the measured count rate divided by 70% to calibrate out the dead time. Using the same setup, the photon detection efficiency (PDE) is measured under three different wavelengths. The laser power is heavily attenuated by a neutral density filter before reaching the SPAD. The result is summarized in Fig. 16(b). At V_{EX} = 1 V, the SPAD has a DCR of 500/second and a PDE of 11.5% at λ = 520 nm.

The timing jitter of SPADs is quantified by the FWHM of its instrumentation response function (IRF), which can be characterized by repeatedly illuminating the device with a δ-like picosecond laser pulse. The time interval between the laser excitation and the SPAD output triggering edge (V_{Cd}, see Fig. 9) is recorded, and the resulting histogram is shown in Fig. 16(c) as the device IRF. The measurement was performed using a 300-fs laser source (IMRA FCPA μJewel D-400, frequency doubled to 522 nm) at 1 MHz repetition rate. The

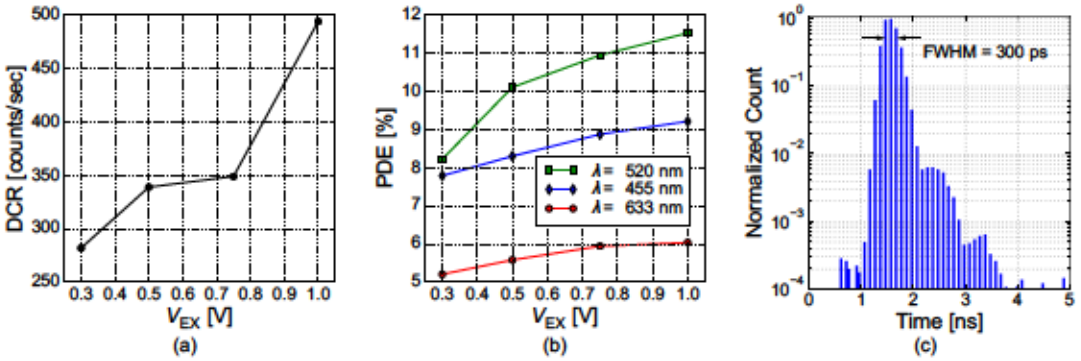

Fig. 16. Measured (a) DCR (b) PDE at different excess biases, and (c) IRF ($V_{EX} = 1$ V).

IRF shows a FWHM = 300 ps, representing a convolved timing uncertainty of the SPAD, readout circuits and the laser synchronization equipments.

VI. Biomolecular Experiment

To perform *in vitro* experiments, samples are dispensed from a pipette onto the chip. Bondwires are protected with a biocompatible UV curable epoxy (EPO-TEK OG116-31). A small amount of the adhesive is dipped from the PCB side, which will flow towards the bondwires and cure in 30 seconds under UV light exposure to avoid contaminating the sensors.

As depicted in Fig. 1, both dielectric and optical signals of the same sample are collected simultaneously, which helps to improve the sensor selectivity by combining results from both sensing modalities. The dielectric signal and the photon timing information were extracted through off-chip analog-to-digital and time-to-digital conversion. All the experiments were performed in the ambient environment with an external voltage regulator. Given that the material dielectric constant is temperature-dependent, temperature control will be needed in a long-term experiment to rule out the temperature induced dielectric drift and achieve the same sensitivity level as a short-term experiment.

A. Protein Denaturation

Denaturation of proteins involves the change of their three-dimensional structures and the loss of functionalities. An *in vitro* experiment is performed to demonstrate that the sensor has (i) a good sensitivity capable of detecting protein structural changes, and (ii) an enhanced selectivity thanks to the use of the dual-modality sensing scheme. Bovine serum albumin (BSA, 66 kDa) is dissolved in PBS to 10% weight concentration and heat-inactivated at 90°C in a sealed container. The protein solution is loaded onto the sensor before and after heating to take measurements (both at room temperature). As shown in Fig. 17, a frequency shift of 444.78 ppm is induced due to BSA unfolding. On the other hand, the unfolding of the enzyme luciferase (LUC, 61 kDa) is not observable because of its extremely low working concentration (0.02% weight concentration in this experiment). Alternatively, LUC catalyzes luciferin oxidation to emit light at its native state only, which allows identifying the denatured LUC with the optical sensor by measuring the luminescence intensity change (Fig. 17). The above experiment is repeated five times and shows consistent results. As depicted by the four clusters in Fig. 17, compared with using a single sensing modality, the four types of proteins (native/denatured BSA/LUC) can be completely distinguished from one another by combining the experimental data from both modalities. In other words, a multimodal strategy improves the overall sensor selectivity.

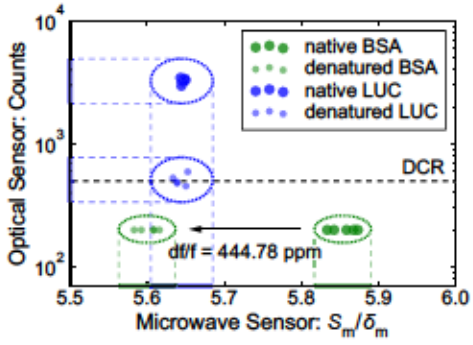

Fig. 17. Protein thermal denaturation, BSA (x-axis) and LUC (xy-axes).

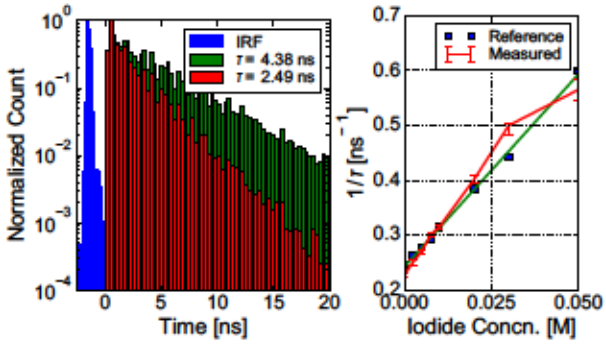

Fig. 18. Rh6G fluorescence lifetime measurement.

B. Fluorescence Lifetime Measurement

In addition to detecting the relative bioluminescent light intensity, the SPAD sensor also measures the absolute fluorescence lifetime to further improve the sensor selectivity. A

TABLE II
COMPARISON WITH OSCILLATOR-BASED REACTANCE SENSORS

Reference	Freq. [GHz]	Type	CMOS Tech.	Approach	Sensitivity [ppm]	Dynamic Range [dB]	Bandwidth [Hz]	Power [mW]
[14]'12	7-9	Dielectric	90 nm	PLL	222*	49.1	-	16.5
[31]'13	10.4	Dielectric	90 nm	PLL	15	72.3	1000	22
[15]'16	16	Dielectric	65 nm	Unilateral Injection + Phase/Field Modulation	0.57	99.3	10	16
[16]'16	60/120	Complex Dielectric	65 nm	Freq. Counting	2.67/2.87	-	100	12.2/34.8
[41]'17	0.98-6	Complex Dielectric	180 nm	Freq. Counting + CDS	2.1	-	4	10 - 24
[18]'18	1.4/3.7	Magnetic	65 nm	Freq. Counting	0.35	>62	1	5
This Work	**42**	**Dielectric**	**28 nm**	**Mutual Injection + Varactor Modulation**	**0.2**	**115**	**1**	**11.5**

*Calculated from reported $\Delta f_{\min} = 2$ MHz.

TABLE III
COMPARISON WITH SPAD IN SUB-100 NM CMOS PROCESS

Reference	Technology	Device Layer	Diameter	Breakdown voltage	DCR [cps] (V_{EX})	PDE (V_{EX})	IRF [ps]
[46]'11	90 nm Bulk	Ndiff−Psub	8 μm	10.4 V	8100 (0.13 V)	12% (0.15 V)	435
[47]'13	65 nm Bulk	Ndiff−Pwell	8 μm	9.1 V	500k (0.25 V)	5.5% (0.25 V)	235
[48]'17	40 nm Bulk*	Pwell−Deep Nwell	5.4 μm	15.5 V	50 (1 V)	30% (1 V)	170
[49]'18	28 nm FD-SOI	Pwell−Deep Nwell	25 μm	9.6 V	28k (0.3 V)	-	-
This Work	**28 nm Bulk**	**Pwell−Deep Nwell**	**6 μm**	**15.3 V**	**500 (1V)**	**11.5% (1 V)**	**300**

*Process tailored for SPAD performance, microlenses included.

fluorescence lifetime standard, rhodamine 6G (Rh6G) iodide solution, is used to characterize the sensor timing accuracy. Rh6G lifetime is varied from 1 to 5 ns with different potassium iodide concentrations (the overall ionic strength maintained at 0.2 M by adjusting the potassium chloride concentration). The measured lifetime values at different iodide concentrations are shown in Fig. 18, which closely match the literature standards in [45], since the device IRF is much narrower compared with the fluorescence exponential decay.

VII. CONCLUSION

Given the predominant role of sensitivity and selectivity in the biosensing applications, this work presents a dual-modality microwave-optical biosensor, which measures the permittivity change, bioluminescence intensity and fluorescence lifetime. A new QVCO-based permittivity sensing architecture is proposed, accompanied by a novel chopping technique to achieve a sensitivity level of 0.2 ppm$/\sqrt{\text{Hz}}$. Table II summaries its performance metrics and compares them with the state-of-the-art oscillator-based reactance sensors. The SPAD-based optical sensor is a first time demonstration in the 28 nm bulk CMOS process. Compared with the prior art, it exhibits better DCR, equivalent PDE and jitter performance without any process modifications, as shown in Table III.

ACKNOWLEDGMENT

The authors would like to thank the TSMC University Shuttle Program for chip fabrication, Ansys HFSS and Integrand EMX for electromagnetic (EM) simulators, and students in the Berkeley Wireless Research Center for useful discussions. Special thanks go to L. Wang and C.P. Grigoropoulos for laser measurement support at Berkeley Laser Thermal Lab.

REFERENCES

[1] W. J. Peveler, M. Yazdani, and V. M. Rotello, "Selectivity and specificity: pros and cons in sensing," *ACS Sens.*, vol. 1, no. 11, pp. 1282–1285, Nov. 2016.

[2] J. Chen, Y. Zheng, Q. Tan, E. Shojaei-Baghini, Y. L. Zhang, J. Li, P. Prasad, L. You, X. Y. Wu, and Y. Sun, "Classification of cell types using a microfluidic device for mechanical and electrical measurement on single cells," *Lab Chip*, vol. 11, no. 18, pp. 3174–3181, Sep. 2011.

[3] A. Y. Zhu, F. Yi, J. C. Reed, H. Zhu, and E. Cubukcu, "Optoelectromechanical multimodal biosensor with graphene active region," *Nano Lett.*, vol. 14, no. 10, pp. 5641–5649, Oct. 2014.

[4] N. Apichitsopa, A. Jaffe, and J. Voldman, "Multiparameter cell-tracking intrinsic cytometry for single-cell characterization," *Lab Chip*, vol. 18, no. 10, pp. 1430–1439, May 2018.

[5] J. Seok Park, S. I. Grijalva, M. K. Aziz, T. Chi, S. Li, M. N. Sayegh, A. Wang, H. Cheol Cho, and H. Wang, "Multi-parametric cell profiling with a CMOS quad-modality cellular interfacing array for label-free fully automated drug screening," *Lab on a Chip*, vol. 18, no. 19, pp. 3037–3050, 2018.

[6] C. M. Lopez, H. S. Chun, S. Wang, L. Berti, J. Putzeys, C. V. D. Bulcke, J. Weijers, A. Firrincieli, V. Reumers, D. Braeken, and N. V. Helleputte, "A multimodal CMOS MEA for high-throughput intracellular action potential measurements and impedance spectroscopy in drug-screening applications," *IEEE Journal of Solid-State Circuits*, vol. 53, no. 11, pp. 3076–3086, Nov. 2018.

[7] V. Viswam, R. Bounik, A. Shadmani, J. Dragas, C. Urwyler, J. A. Boos, M. E. J. Obien, J. Müller, Y. Chen, and A. Hierlemann, "Impedance spectroscopy and electrophysiological imaging of cells with a high-density CMOS microelectrode array system," *IEEE Transactions on Biomedical Circuits and Systems*, vol. 12, no. 6, pp. 1356–1368, Dec. 2018.

[8] M. A. Al-Rawhani, C. Hu, C. Giagkoulovits, V. Annese, B. C. Cheah, J. M. Beeley, S. Velugotla, C. Accarino, J. Grant, S. Mitra, M. Barrett, S. Cochran, and D. Cumming, "Multimodal integrated sensor platform for rapid biomarker detection," *IEEE Transactions on Biomedical Engineering*, Jun. 2019.

[9] B. Miccoli, C. M. Lopez, E. Goikoetxea, J. Putzeys, M. Sekeri, O. Krylychkina, S.-W. Chang, A. Firrincieli, A. Andrei, V. Reumers, and D. Braeken, "High-density electrical recording and impedance imaging with a multi-modal CMOS multi-electrode array chip," *Front. Neurosci.*, vol. 13, 2019.

[10] D. Jung, J. S. Park, G. V. Junek, S. I. Grijalva, S. R. Kumashi, A. Wang, S. Li, H. C. Cho, and H. Wang, "A 21952-pixel multi-modal CMOS

cellular sensor array with 1568-pixel parallel recording and 4-point impedance sensing," in *2019 Symposium on VLSI Circuits*, Jun. 2019, pp. C62–C63.

[11] J. Chien and A. M. Niknejad, "Oscillator-based reactance sensors with injection locking for high-throughput flow cytometry using microwave dielectric spectroscopy," *IEEE Journal of Solid-State Circuits*, vol. 51, no. 2, pp. 457–472, Feb. 2016.

[12] H. Eltoukhy, K. Salama, and A. E. Gamal, "A 0.18-μm CMOS bioluminescence detection lab-on-chip," *IEEE Journal of Solid-State Circuits*, vol. 41, no. 3, pp. 651–662, Mar. 2006.

[13] A. Manickam, R. Singh, M. W. McDermott, N. Wood, S. Bolouki, P. Naraghi-Arani, K. A. Johnson, R. G. Kuimelis, G. Schoolnik, and A. Hassibi, "A fully integrated CMOS fluorescence biochip for DNA and RNA testing," *IEEE Journal of Solid-State Circuits*, vol. 52, no. 11, pp. 2857–2870, Nov. 2017.

[14] A. A. Helmy, H. Jeon, Y. Lo, A. J. Larsson, R. Kulkarni, J. Kim, J. Silva-Martinez, and K. Entesari, "A self-sustained CMOS microwave chemical sensor using a frequency synthesizer," *IEEE Journal of Solid-State Circuits*, vol. 47, no. 10, pp. 2467–2483, Oct. 2012.

[15] J. Chien and A. M. Niknejad, "Design and analysis of chopper stabilized injection-locked oscillator sensors employing near-field modulation," *IEEE Journal of Solid-State Circuits*, vol. 51, no. 8, pp. 1851–1865, Aug. 2016.

[16] T. Mitsunaka, D. Sato, N. Ashida, A. Saito, K. Iizuka, T. Suzuki, Y. Ogawa, and M. Fujishima, "CMOS biosensor IC focusing on dielectric relaxations of biological water with 120 and 60 GHz oscillator arrays," *IEEE Journal of Solid-State Circuits*, vol. 51, no. 11, pp. 2534–2544, Nov. 2016.

[17] P. Hillger, R. Jain, J. Grzyb, W. Förster, B. Heinemann, G. MacGrogan, P. Mounaix, T. Zimmer, and U. R. Pfeiffer, "A 128-pixel system-on-a-chip for real-time super-resolution terahertz near-field imaging," *IEEE Journal of Solid-State Circuits*, vol. 53, no. 12, pp. 3599–3612, Dec. 2018.

[18] C. Sideris, P. P. Khial, and A. Hajimiri, "Design and implementation of reference-free drift-cancelling CMOS magnetic sensors for biosensing applications," *IEEE Journal of Solid-State Circuits*, vol. 53, no. 11, pp. 3065–3075, Nov. 2018.

[19] C. Wang and R. Han, "Dual-terahertz-comb spectrometer on CMOS for rapid, wide-range gas detection with absolute specificity," *IEEE Journal of Solid-State Circuits*, vol. 52, no. 12, pp. 3361–3372, Dec. 2017.

[20] J. M. Pavia, M. Scandini, S. Lindner, M. Wolf, and E. Charbon, "A 1 $\times$ 400 backside-illuminated SPAD sensor with 49.7 ps resolution, 30 pJ/sample TDCs fabricated in 3D CMOS technology for near-infrared optical tomography," *IEEE Journal of Solid-State Circuits*, vol. 50, no. 10, pp. 2406–2418, Oct. 2015.

[21] A. Boukhayma, A. Peizerat, and C. Enz, "A sub-0.5 electron read noise VGA image sensor in a standard CMOS process," *IEEE Journal of Solid-State Circuits*, vol. 51, no. 9, pp. 2180–2191, Sep. 2016.

[22] C. Veerappan and E. Charbon, "A low dark count p-i-n diode based SPAD in CMOS technology," *IEEE Transactions on Electron Devices*, vol. 63, no. 1, pp. 65–71, Jan. 2016.

[23] L. Zhang, A. Ameri, M. Anwar, and A. M. Niknejad, "A microwave-optical biosensor with 5.4ppm label/reference-free long-term stability and single photon sensitivity in 28nm bulk CMOS," in *2019 IEEE Custom Integrated Circuits Conference (CICC)*, Apr. 2019, pp. 1–4.

[24] M. Samet, V. Levchenko, G. Boiteux, G. Seytre, A. Kallel, and A. Serghei, "Electrode polarization vs. Maxwell-Wagner-Sillars interfacial polarization in dielectric spectra of materials: characteristic frequencies and scaling laws," *The Journal of Chemical Physics*, vol. 142, no. 19, p. 194703, May 2015.

[25] C. A. E. Little, N. D. Orloff, I. E. Hanemann, C. J. Long, V. M. Bright, and J. C. Booth, "Modeling electrical double-layer effects for microfluidic impedance spectroscopy from 100 kHz to 110 GHz," *Lab Chip*, vol. 17, no. 15, pp. 2674–2681, Jul. 2017.

[26] D. E. Schwartz, E. Charbon, and K. L. Shepard, "A single-photon avalanche diode array for fluorescence lifetime imaging microscopy," *IEEE Journal of Solid-State Circuits*, vol. 43, no. 11, pp. 2546–2557, Nov. 2008.

[27] A. D. Mora, A. Tosi, F. Zappa, S. Cova, D. Contini, A. Pifferi, L. Spinelli, A. Torricelli, and R. Cubeddu, "Fast-gated single-photon avalanche diode for wide dynamic range near infrared spectroscopy," *IEEE Journal of Selected Topics in Quantum Electronics*, vol. 16, no. 4, pp. 1023–1030, Jul. 2010.

[28] Y. Maruyama, J. Blacksberg, and E. Charbon, "A 1024 $\times$ 8, 700-ps time-gated SPAD line sensor for planetary surface exploration with laser Raman spectroscopy and LIBS," *IEEE Journal of Solid-State Circuits*, vol. 49, no. 1, pp. 179–189, Jan. 2014.

[29] U. Kaatze, "Complex permittivity of water as a function of frequency and temperature," *J. Chem. Eng. Data*, vol. 34, no. 4, pp. 371–374, Oct. 1989.

[30] H. Wang, S. Kosai, C. Sideris, and A. Hajimiri, "An ultrasensitive CMOS magnetic biosensor array with correlated double counting noise suppression," in *2010 IEEE MTT-S International Microwave Symposium*, May 2010, pp. 616–619.

[31] O. Elhadidy, M. Elkholy, A. A. Helmy, S. Palermo, and K. Entesari, "A CMOS fractional-*N* PLL-based microwave chemical sensor with 1.5% permittivity accuracy," *IEEE Transactions on Microwave Theory and Techniques*, vol. 61, no. 9, pp. 3402–3416, Sep. 2013.

[32] A. Chu, B. Schlecker, K. Lips, M. Ortmanns, and J. Anders, "An 8-channel 13GHz ESR-on-a-Chip injection-locked VCO-array achieving 200μM-concentration sensitivity," in *2018 IEEE International Solid - State Circuits Conference - (ISSCC)*, Feb. 2018, pp. 354–356.

[33] M. Gal-Katziri and A. Hajimiri, "Analysis and design of coupled inductive bridges for magnetic sensing applications," *IEEE Journal of Solid-State Circuits*, pp. 1–12, 2019.

[34] H. Wang, C. Weng, and A. Hajimiri, "Phase noise and fundamental sensitivity of oscillator-based reactance sensors," *IEEE Transactions on Microwave Theory and Techniques*, vol. 61, no. 5, pp. 2215–2229, May 2013.

[35] R. Adler, "A study of locking phenomena in oscillators," *Proceedings of the IRE*, vol. 34, no. 6, pp. 351–357, Jun. 1946.

[36] R. A. York and R. C. Compton, "Quasi-optical power combining using mutually synchronized oscillator arrays," *IEEE Transactions on Microwave Theory and Techniques*, vol. 39, no. 6, pp. 1000–1009, Jun. 1991.

[37] R. A. York, "Nonlinear analysis of phase relationships in quasi-optical oscillator arrays," *IEEE Transactions on Microwave Theory and Techniques*, vol. 41, no. 10, pp. 1799–1809, Oct. 1993.

[38] B. Razavi, "A study of injection locking and pulling in oscillators," *IEEE Journal of Solid-State Circuits*, vol. 39, no. 9, pp. 1415–1424, Sep. 2004.

[39] Heng-Chia Chang, Xudong Cao, U. K. Mishra, and R. A. York, "Phase noise in coupled oscillators: theory and experiment," *IEEE Transactions on Microwave Theory and Techniques*, vol. 45, no. 5, pp. 604–615, May 1997.

[40] L. Zhang, N. Kuo, and A. M. Niknejad, "A 37.5-45 GHz superharmonic-coupled QVCO with tunable phase accuracy in 28 nm CMOS," *IEEE Journal of Solid-State Circuits*, pp. 1–11, 2019.

[41] M. Elkholy and K. Entesari, "A wideband low-power LC-DCO-based complex dielectric spectroscopy system in 0.18-μm CMOS," *IEEE Transactions on Microwave Theory and Techniques*, vol. 65, no. 11, pp. 4461–4474, Nov. 2017.

[42] A. Rochas, M. Gani, B. Furrer, P. A. Besse, R. S. Popovic, G. Ribordy, and N. Gisin, "Single photon detector fabricated in a complementary metal-oxide-semiconductor high-voltage technology," *Review of Scientific Instruments*, vol. 74, no. 7, pp. 3263–3270, Jul. 2003.

[43] A. Mirzaei and H. Darabi, "Mutual pulling between two oscillators," *IEEE Journal of Solid-State Circuits*, vol. 49, no. 2, pp. 360–372, Feb. 2014.

[44] J. Chien, M. Anwar, Erh-Chia Yeh, L. P. Lee, and A. M. Niknejad, "A 6.5/11/17.5/30-GHz high throughput interferometer-based reactance sensors using injection-locked oscillators and ping-pong nested chopping," in *2014 Symposium on VLSI Circuits Digest of Technical Papers*, Jun. 2014, pp. 1–2.

[45] Q. S. Hanley, V. Subramaniam, D. J. Arndt-Jovin, and T. M. Jovin, "Fluorescence lifetime imaging: multi-point calibration, minimum resolvable differences, and artifact suppression," *Cytometry*, vol. 43, no. 4, pp. 248–260, 2001.

[46] M. A. Karami, H. Yoon, and E. Charbon, "Single-photon avalanche diodes in sub-100nm standard CMOS technologies," 2011.

[47] E. Charbon, H. Yoon, and Y. Maruyama, "A Geiger mode APD fabricated in standard 65nm CMOS technology," in *2013 IEEE International Electron Devices Meeting*, Dec. 2013, pp. 27.5.1–27.5.4.

[48] S. Pellegrini, B. Rae, A. Pingault, D. Golanski, S. Jouan, C. Lapeyre, and B. Mamdy, "Industrialised SPAD in 40 nm technology," in *2017 IEEE International Electron Devices Meeting (IEDM)*, Dec. 2017, pp. 16.5.1–16.5.4.

[49] T. C. de Albuquerque, F. Calmon, R. Clerc, P. Pittet, Y. Benhammou, D. Golanski, S. Jouan, D. Rideau, and A. Cathelin, "Integration of SPAD in 28nm FDSOI CMOS technology," in *2018 48th European Solid-State Device Research Conference (ESSDERC)*, Sep. 2018, pp. 82–85.

Luya Zhang (S'15) received the B.S. degree in microelectronics (with a double major in economics) from Peking University, Beijing, China, in 2015, and the master's degree in electrical engineering and computer sciences from the University of California, Berkeley, CA, USA, in 2018, where she is currently pursuing the Ph.D. degree.

Her current research interests include the development of microwave/mm-wave frequency impedance spectroscopy for biomedical applications, focusing on circuit and algorithmic techniques to achieve low power and high performance sensing.

Ali M. Niknejad (S'93-M'00-SM'10-F'13) received the B.S.E.E. degree from the University of California, Los Angeles, CA, USA, in 1994, and the master's and Ph.D. degrees in electrical engineering from the University of California, Berkeley, CA, USA, in 1997 and 2000, respectively.

He is currently a Professor with the Department of Electrical Engineering and Computer Sciences at University of California, Berkeley and a Faculty Director of the Berkeley Wireless Research Center (BWRC). He is also the Associate Director of Center for Converged TeraHertz Communications and Sensing (ComSenTer). He is a co-founder of HMicro (LifeSignals) and inventor of REACH™ technology, which has the potential to deliver robust wireless solutions to the healthcare industry. He is also co-founder of RF Pixels, a 5G technology startup, and is on the board of CalTerah, a CMOS radar technology start-up company in Shanghai. He is also on the technical advisory board of Zendar, a Berkeley based high resolution radar imaging start-up.

Dr. Niknejad was the co-recipient of the 2017 IEEE Transactions On Circuits And Systems Darlington Best Paper Award, the 2017 Most Frequently Cited Paper Award from 2010 to 2016 of the Symposium on Very Large-Scale Integration (VLSI) Circuits, the CICC 2015 Best Invited Paper Award, and the 2012 ASEE Frederick Emmons Terman Award for his research and textbook on electromagnetics and RF integrated circuits. He was the co-recipient of the 2013 Jack Kilby Award for Outstanding Student Paper for the work on an efficient quadrature digital spatial modulator at 60 GHz, the 2010 Jack Kilby Award for Outstanding Student Paper for the work on a 90-GHz pulser with 30 GHz of bandwidth for medical imaging, and the Outstanding Technology Directions Paper of ISSCC 2004 for co-developing a modeling approach for devices up to 65 GHz.